Electronic Supplementary Information

Photocatalytic CO_2 reduction to C_{2+} products by metal-organic framework composited with facet engineered Pd nanoparticles

Xiang-Yu Lu,[a]‡ Qiang Zhou,[bc]‡ Xiao-Yu Zhang,[a] Ya Zhang,[a] Feng Gong[b]* and Wei-Yin Sun[a]*

‡ Equal contribution for this work.

[a] Coordination Chemistry Institute, State Key Laboratory of Coordination Chemistry, School of Chemistry and Chemical Engineering, Nanjing National Laboratory of Microstructures, Collaborative Innovation Center of Advanced Microstructures, Nanjing University, Nanjing 210023, China. E-mail: sunwy@nju.edu.cn(W.-Y. Sun)

[b] Key Laboratory of Energy Thermal Conversion and Control of Ministry of Education, School of Energy and Environment, Southeast University, Nanjing 210096, China. E-mail: gongfeng@seu.edu.cn (F. Gong)

[c] School of Engineering, The University of Tokyo, Tokyo 113-8656, Japan

S1 Materials

All commercially available chemicals and solvents are of reagent grade and were used as received without further purification.

S2 Calculation of isosteric enthalpy of adsorption

Isosteric enthalpy of adsorption (*Qst*) was calculated from CO_2 adsorption isotherms measured at 273 and 298 K. The isotherms were fitted to a virial equation (**Equation S1**):

$$lnP = lnN + \frac{1}{T}\Sigma_{i=0}^{m} a^i N^i + \Sigma_{i=0}^{n} b^i N^i \qquad \text{(S1)}$$

Here, P is the pressure expressed in Torr, N is the amount adsorbed in mmol/g, T is the

temperature in K, a^i and b^i are virial coefficients, and *m*, *n* represent the number of coefficients required to adequately describe the isotherms (*m* and *n* were gradually increased until the contribution of extra added *a* and *b* coefficients were deemed to be statistically insignificant towards the overall fit, and the average value of the squared deviations from the experimental values was minimized). The values of the virial coefficients a^0 through a^m were then used to calculate the isosteric heat of adsorption using the following expression (**Equation S2**):

$$Q_{st} = -R\Sigma_{i=0}^{m} a^i N^i \quad \text{(S2)}$$

S3 Characterization methods

Powder X-ray diffraction (PXRD) data were collected on a Bruker D8 Advance X-ray diffractometer with Cu Kα (λ=1.5418 Å) radiation. FT-IR ATR spectra within 4000-400 cm^{-1} were recorded on an infrared spectrophotometer (Bruker Tensor II) with a diamond ATR module. X-ray photoelectron spectroscopy (XPS) was performed on Thermo ESCALAB 250XI with aluminum Kα radiation. Scanning electron microscopy (SEM) images were obtained on a Hitachi S-4800 SEM at 5 kV. Transmission electron microscopy (TEM) and high-resolution transmission electron microscopy (HRTEM) images were achieved on JEM-2100 with an acceleration voltage of 100 kV. The high-angle annular dark-field scanning transmission electron microscopy (HAADF-STEM) images and STEM-EDX elemental mappings were collected on FEI Talos F200X (Thermo Fisher Scientific). The N_2 and CO_2 adsorption isotherms were measured on a Micromeritics ASAP 2020 system using a standard volumetric technique up to saturated pressure. Before adsorption measurements, all samples were activated and degassed at 180 ℃ for 6 h. UV-vis diffuse reflectance spectra (DRS) were recorded on a Shimadzu UV-3600 spectrophotometer in the wavelength range of 200 - 800 nm, and a white standard of $BaSO_4$ was used as a reference. Photoluminescence (PL) spectra were measured on a Perkin Elmer LS-55 fluorescence spectrophotometer. Time-resolved fluorescence decay spectra were obtained at room temperature on a HORIBA Jobin Yvon FL-3 spectrometer.

Transient photocurrent responses were performed using a CHI730E electrochemical workstation (Chen Hua Instrument, Shanghai, China). The electrochemical impedance spectroscopy (EIS) and Mott-Schottky tests were performed on the Zahner electrochemical workstation (IM6ex, Zahner Scientific Instruments, German).

S4 Electrochemical tests

5.0 mg catalysts and 20 μL of Nafion (Du Pont) were added into 1 mL isopropanol to prepare ink through ultrasonic processing for preparing the working electrode. A standard three-electrode system with a Pt wire as the counter electrode and an Ag/AgCl as the reference electrode was used. A 0.2 M Na_2SO_4 solution was used as the electrolyte. The Mott-Schottky test was performed on the Zahner electrochemical workstation with photocatalyst-coated ITO as a working electrode, which was prepared by dropping 200 μL of ink onto the ITO glass with an active area of 1 cm^2 and dried on a heating plate to form a tight-packed layer. The measurements were carried out under frequencies 500, 1000 and 1500 Hz. The electrochemical impedance spectroscopy (EIS) was performed on the Zahner electrochemical workstation with photocatalyst-coated carbon paper as a working electrode, which was prepared by dropping the above ink (200 μL) onto the surface of the carbon paper and dried at 100 ºC. The measurements were carried out with a bias potential of -0.1 V with a frequency range from 10^{-2} to 10^5 Hz under a nitrogen atmosphere. Photocurrent measurements were recorded on the CHI 730E electrochemical workstation with a photocatalyst-coated ITO as a working electrode, prepared with the above method. The measurements were carried out under chopped light at 0.5 V.

S5 *In Situ* FT-IR measurements

In situ FT-IR measurements were conducted using the Thermo Fisher is50 FT-IR spectrometer equipped with an *in situ* diffuse reflectance cell (Harrick). First, the 5 mg photocatalyst was vacuum treated, and then CO_2 was introduced into a reactor containing 2 ml ultra-pure water and adsorbed in the dark for 30 min. After that, the photocatalyst was irradiated for 60 min, and FT-IR spectra were recorded repeatedly at an interval of 10 min.

S6 Computational method

All spin-polarized computations were performed under the framework of density functional theory (DFT) employing Vienna ab-initio simulation package (VASP).[1] Perdew-Burke-Ernzerhof (PBE) functional among a generalized gradient approximation (GGA) was introduced to describe the exchange and correlation effect of the electron.[2] The projector augmented wave (PAW) method was employed to describe the electron-ion interaction.[3,4] The kinetic energy cutoff for plane wave was set to 400 eV. The Brillouin zone was sampled by 2 × 2 × 1 grid for Pd(100)/MIL-100 and 3× 3× 1 grid for Pd(111)/MIL-100. The criterion of structure relaxation was set to 10^{-4} eV for total energy and 0.05 eV/Å for the force of each atom. DFT-D3 method was employed for the correction of vdWs force. The Pd(100)/MIL-100(Fe) and Pd(111)/MIL-100(Fe) were modeled by combining the single unit of MIL-100(Fe) with 3-layer 3 × 3 supercell of Pd(100) and 2 × 2 supercell of Pd(111), where the single unit of MIL-100(Fe) was fixed as the substrate. A 20 Å vacuum layer was introduced to avoid the interaction between different layers. The calculation of Gibbs free energy change (ΔG) for each elementary reaction was based on the computational hydrogen electrode model proposed by Nørskov et al. given by:

$$\Delta G = \Delta E + \Delta ZPE - T\Delta S + eU + \Delta G_{pH} \quad \text{(S3)}$$

where ΔE is the difference of calculated DFT energy. ZPE is zero-point energy calculated from the vibrational frequency. T was set as 300 K and the entropy ΔS was computed by fixing the catalyst base, where the entropy value of gas molecules was obtained from a NIST database. ΔGpH was the contribution to ΔG at a certain pH value, given by: $\Delta G_{pH} = kBT \times pH \times ln10 = 0.06pH$.

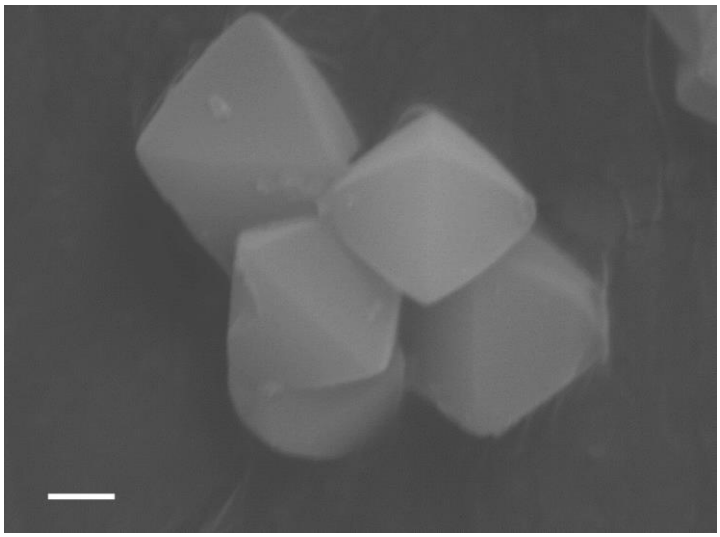

Fig. S1. SEM image of MIL-100(Fe) (scale bar: 1 μm).

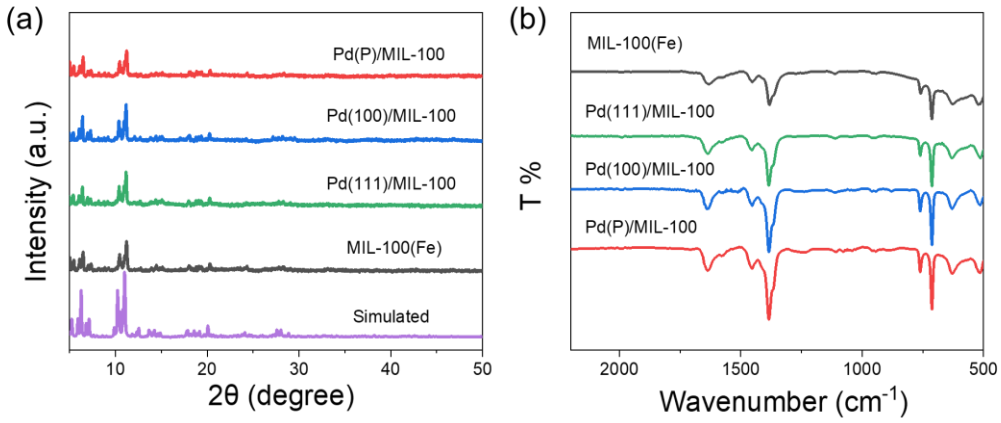

Fig. S2. PXRD (a) and FT-IR (b) spectra of varied catalysts.

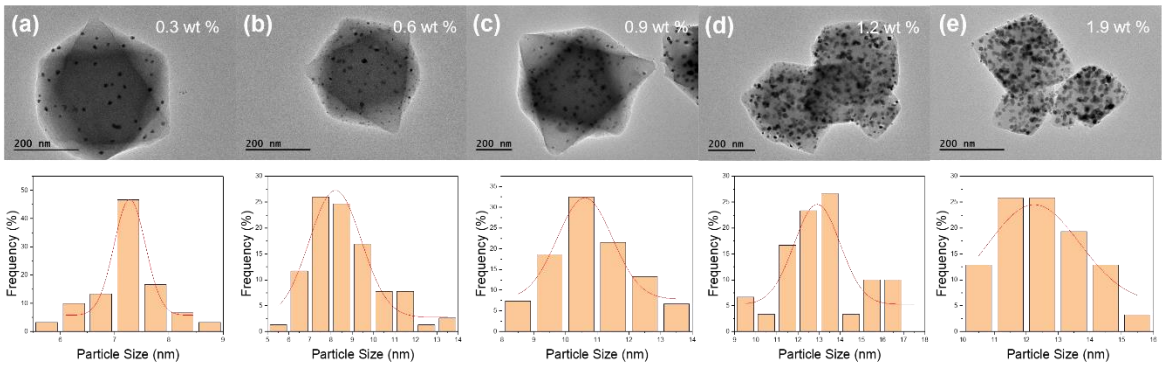

Fig. S3. TEM images with different Pd mass loading of Pd(111)/MIL-100. (a) 0.3 wt %; (b) 0.6 wt %; (c) 0.9 wt %; (d) 1.2 wt %; (e)1.9wt%. The bottom figure shows the corresponding particle size distribution.

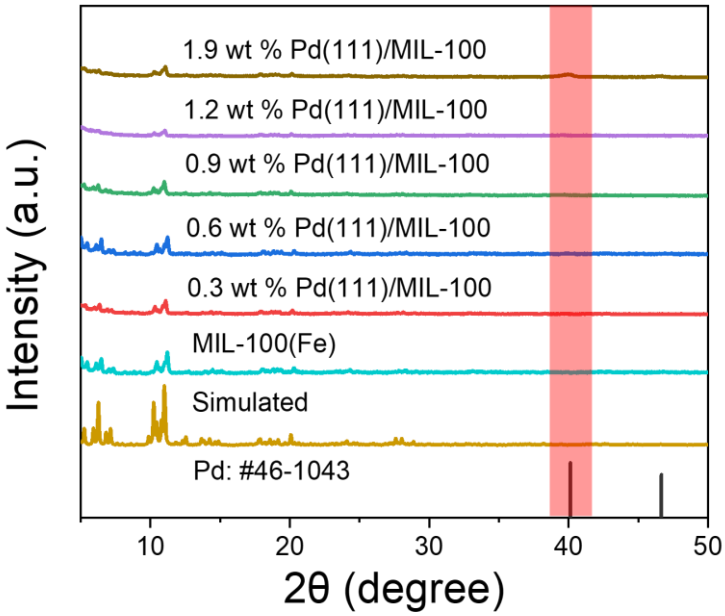

Fig. S4. PXRD patterns with different Pd mass loading of Pd(111)/MIL-100.

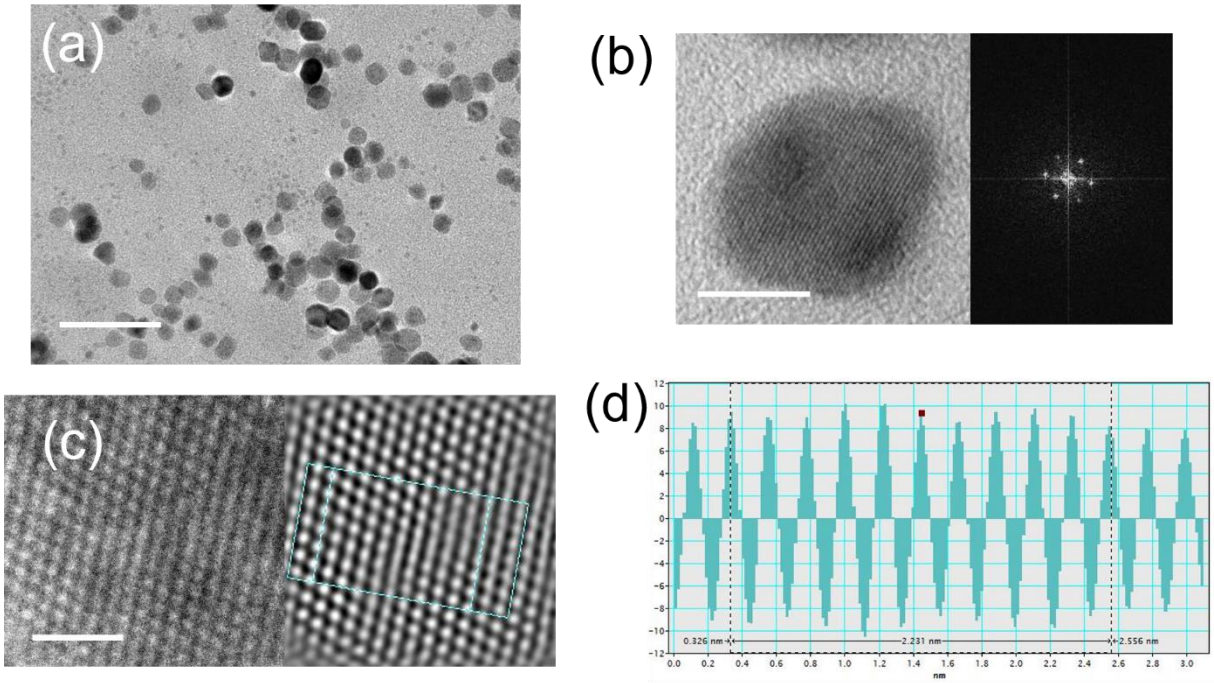

Fig. S5. (a) TEM image of Pd(111)NPs obtained by chemical reduction method (scale bar: 50 nm); (b) HRTEM image of Pd(111) NPs. The illustration on the right shows the corresponding FFT pattern (scale bar: 5 nm). (c) HRTEM with further amplification. The illustration on the right shows the mathematical image obtained after the inverse Fourier transform (scale bar: 1 nm). (d) Particle size distribution obtained in the viewfinder frame. The average lattice spacing is 0.22 nm by the ten-point method.

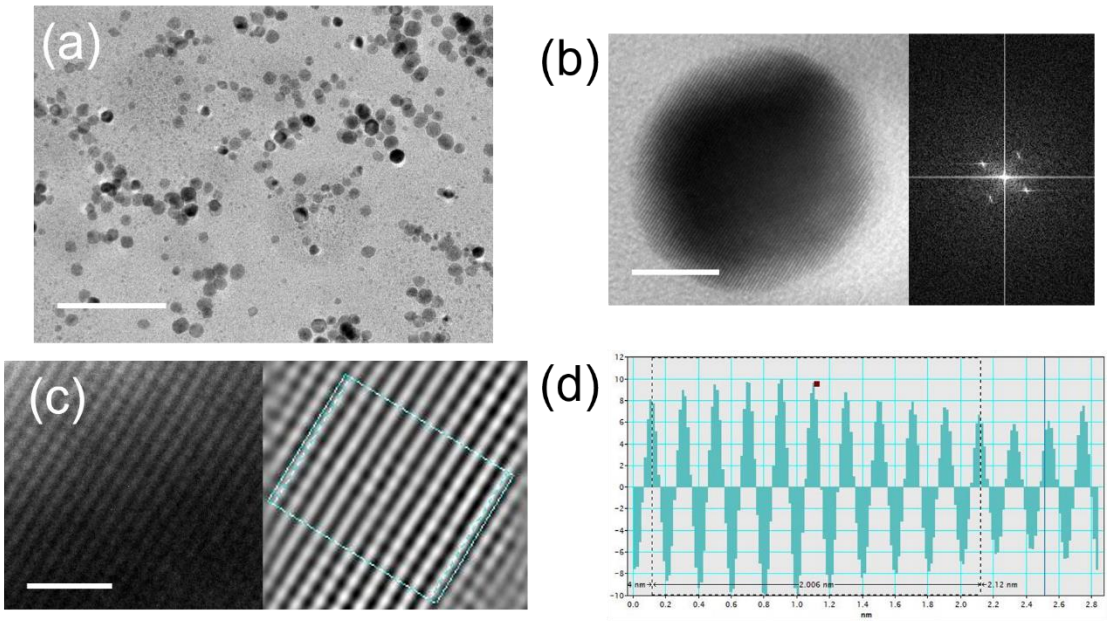

Fig. S6. (a) TEM image of Pd(100) NPs obtained by chemical reduction method (scale bar: 50 nm). (b) HRTEM image of Pd(100) NPs. The illustration on the right shows the corresponding FFT patterns (scale bar: 5 nm). (c) HRTEM with further amplification. The illustration on the right shows the mathematical image obtained after the inverse Fourier transform (scale bar: 1 nm). (d) Particle size distribution obtained in the viewfinder frame. The average lattice spacing is 0.20 nm by the ten-point method.

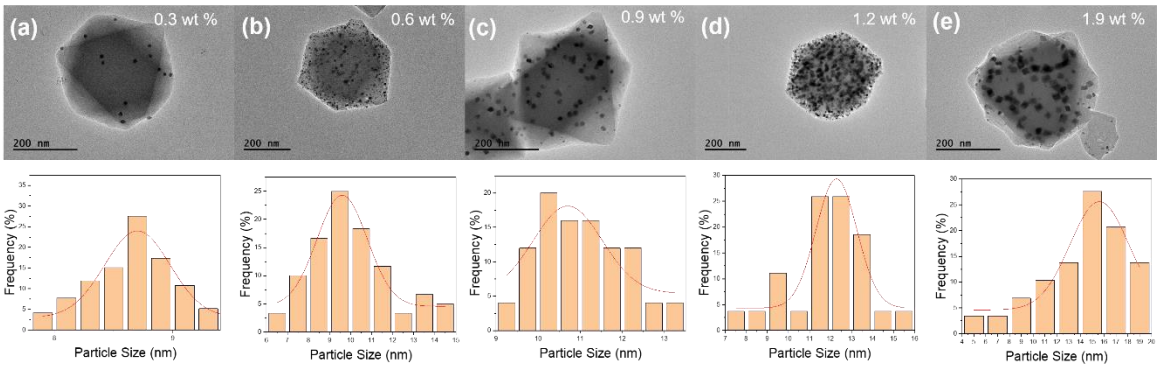

Fig. S7. TEM images with different Pd mass loading of Pd(100)/MIL-100. (a) 0.3 wt %; (b) 0.6 wt %; (c) 0.9 wt %; (d) 1.2 wt %; (e)1.9wt%. The bottom figure shows the corresponding particle size distribution.

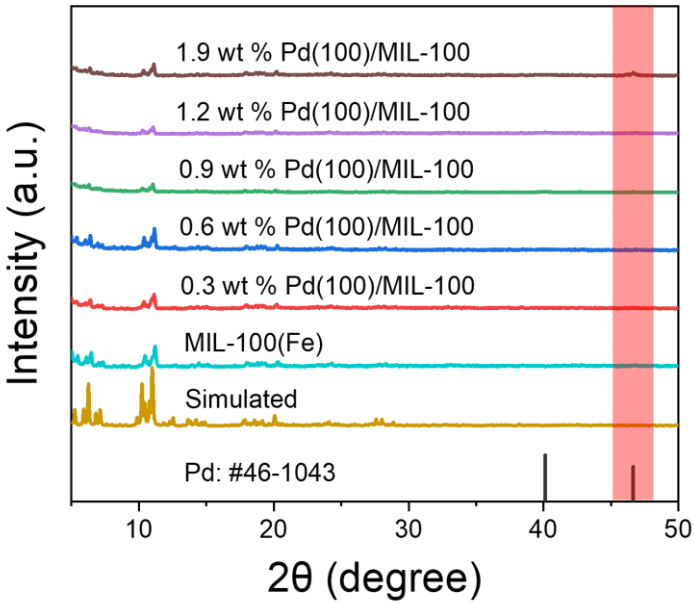

Fig. S8. PXRD patterns with different Pd mass loading of Pd(100)/MIL-100.

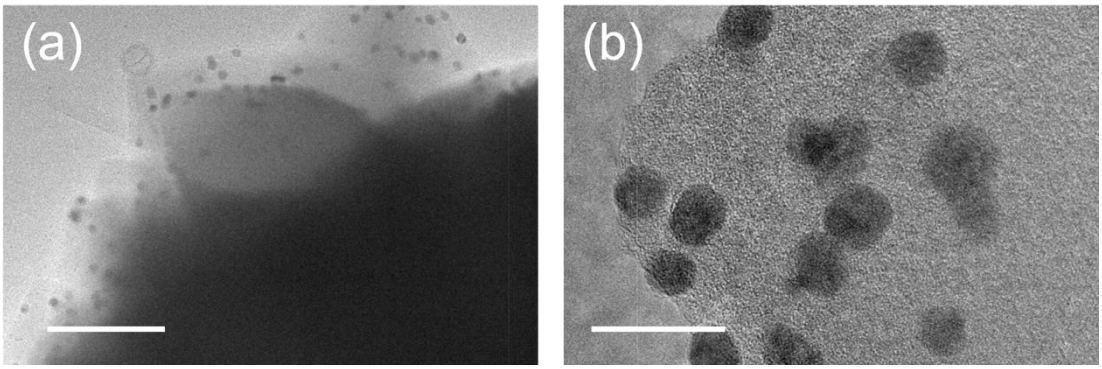

Fig. S9. (a) TEM image of Pd(P)/MIL-100 prepared by photoreduction method (scale bar: 100 nm). (b) HRTEM image (scale bar: 20 nm).

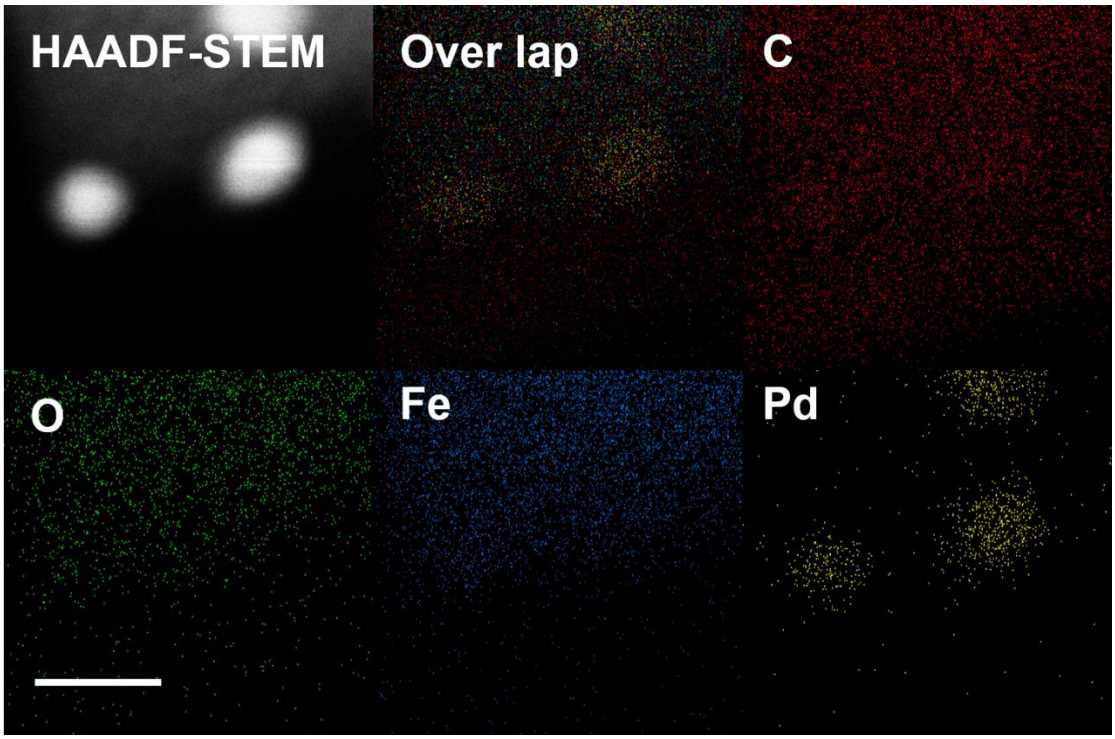

Fig. S10. HAADF-STEM image and corresponding elemental mapping images of Pd(111)/MIL-100 at high magnification (scale bar: 10 nm).

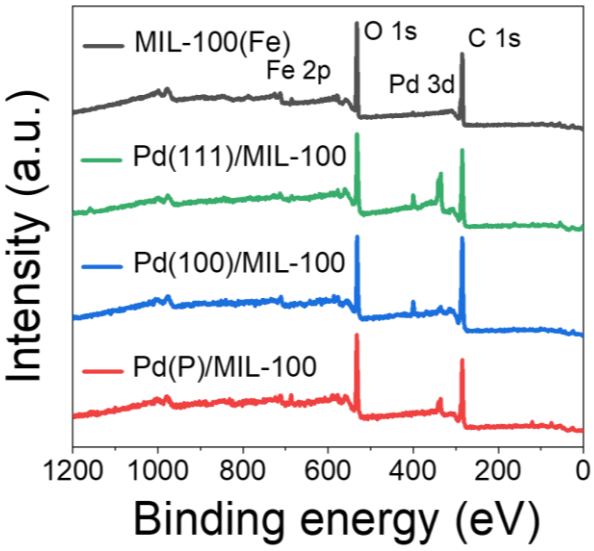

Fig. S11. XPS survey spectra of varied catalysts.

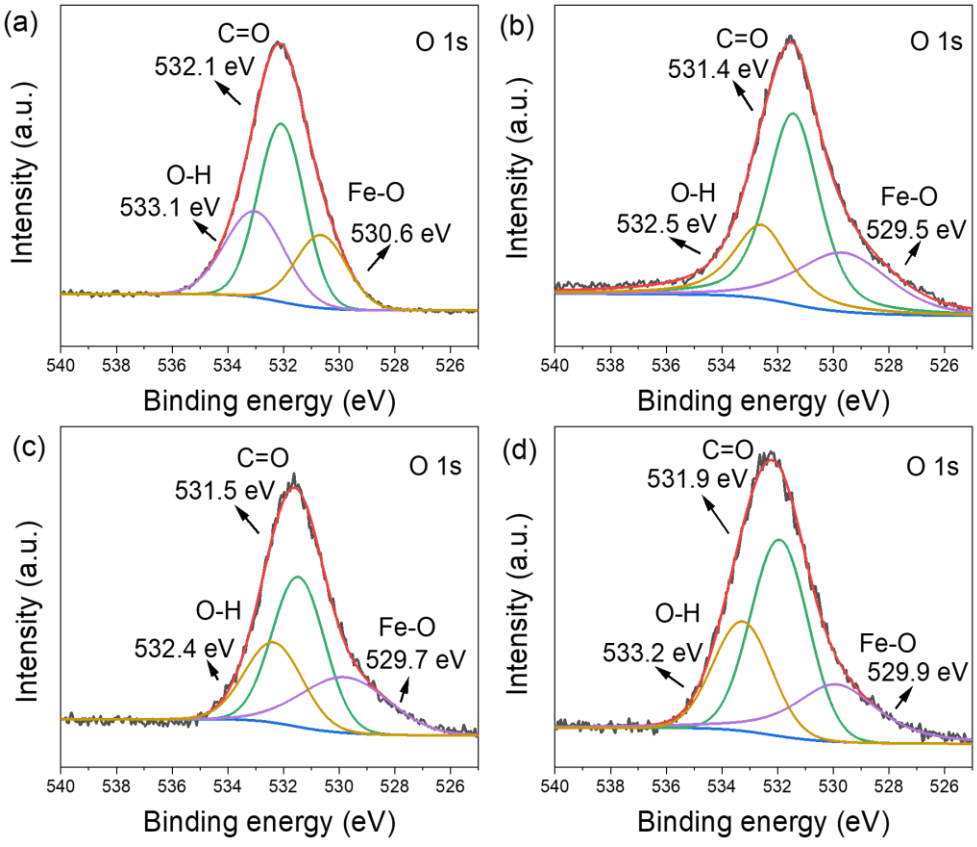

Fig. S12. High-resolution O 1s XPS spectra of varied catalysts. (a) MIL-100(Fe); (b) Pd(111)/MIL-100; (c) Pd(100)/MIL-100; (d) Pd(P)/MIL-100.

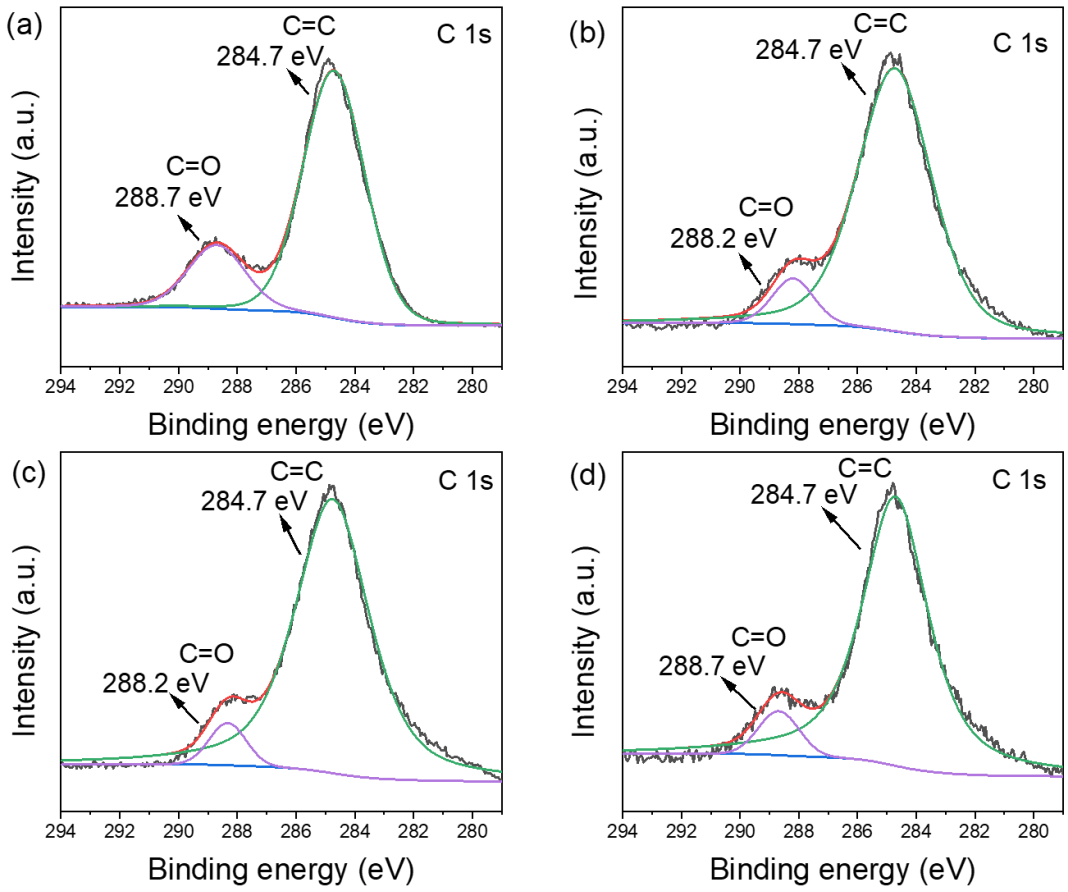

Fig. S13. High-resolution C 1s XPS spectra of varied catalysts. (a) MIL-100(Fe); (b) Pd(111)/MIL-100; (c) Pd(100)/MIL-100; (d) Pd(P)/MIL-100.

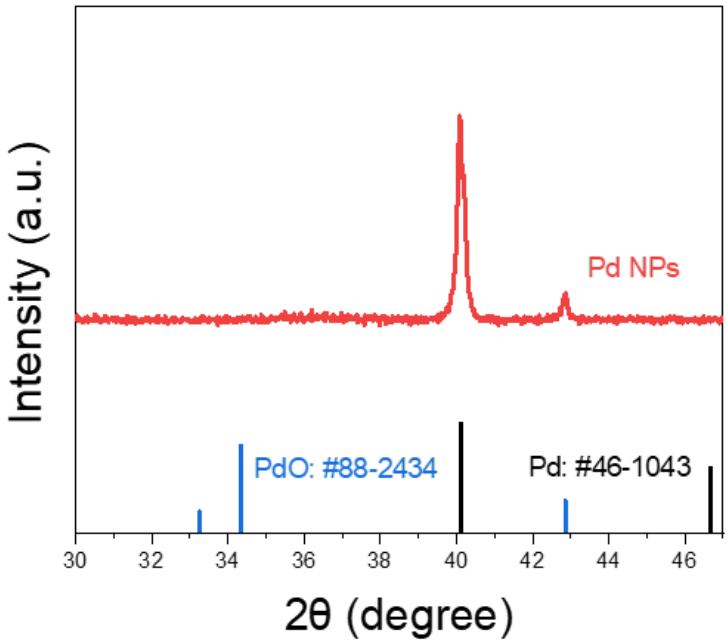

Fig. S14. PXRD pattern of Pd NPs.

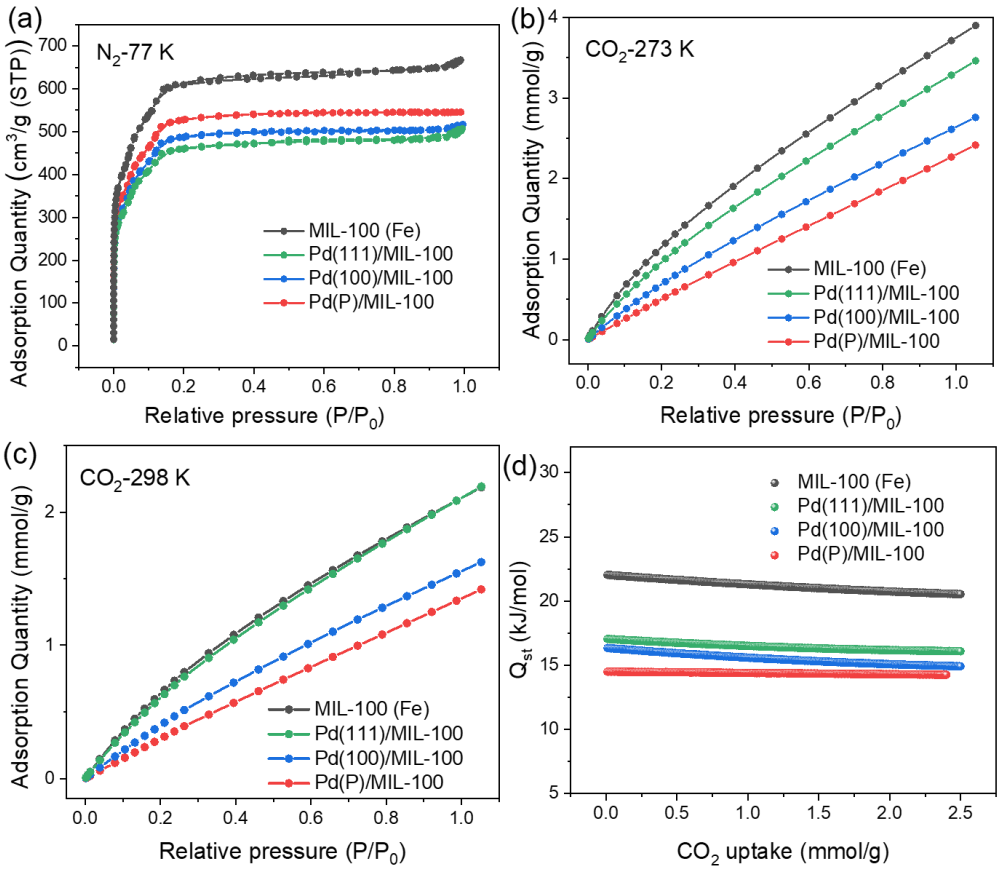

Fig. S15. Gas adsorption isotherms and CO_2 adsorption enthalpy curves of varied catalysts. (a) N_2 adsorption isotherms at 77 K, (b, c) CO_2 adsorption isotherms at 273 and 298 K, and (d) CO_2 adsorption enthalpy curves.

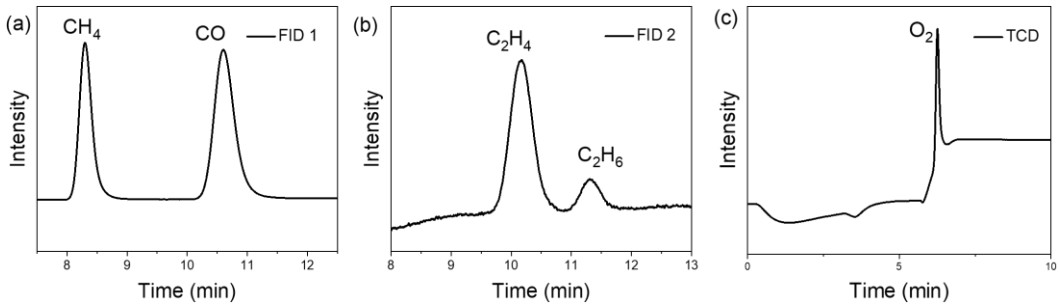

Fig. S16. Typical gas chromatogram observed during the irradiation: (a) FID1 detector for CH_4 and CO monitoring; (b) FID2 detector for C_2H_4 and C_2H_6 monitoring; (c) TCD detector for H_2 and O_2 detecting, which showed no H_2 detected.

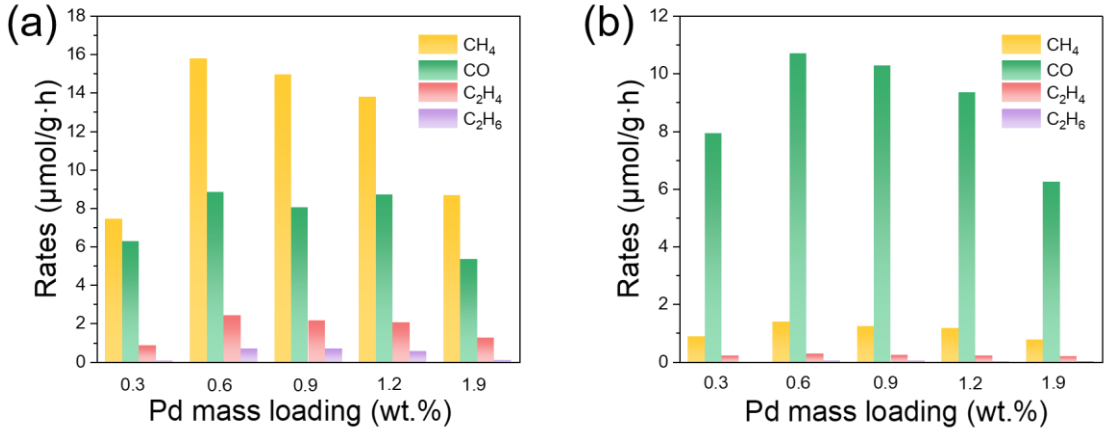

Fig. S17. Comparison of photocatalytic CO_2 performance of Pd/MIL-100 with different Pd mass loading. (a) Pd(111)/MIL-100; (b) Pd(100)/MIL-100.

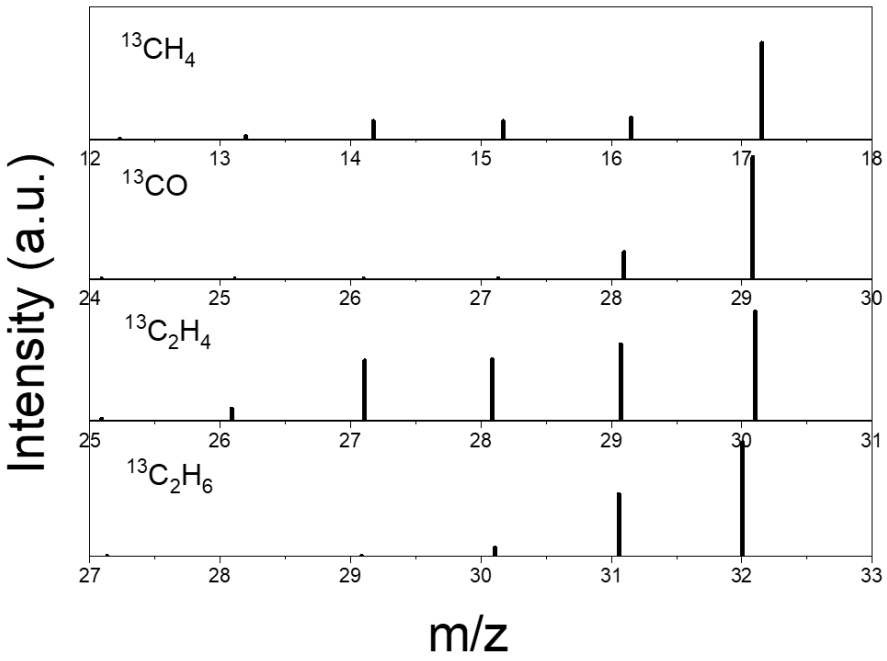

Fig. S18. GC-MS spectra of the produced $^{13}CH_4$, ^{13}CO, $^{13}C_2H_4$ and $^{13}C_2H_6$ from the photocatalytic $^{13}CO_2$ reduction on Pd(111)/MIL-100.

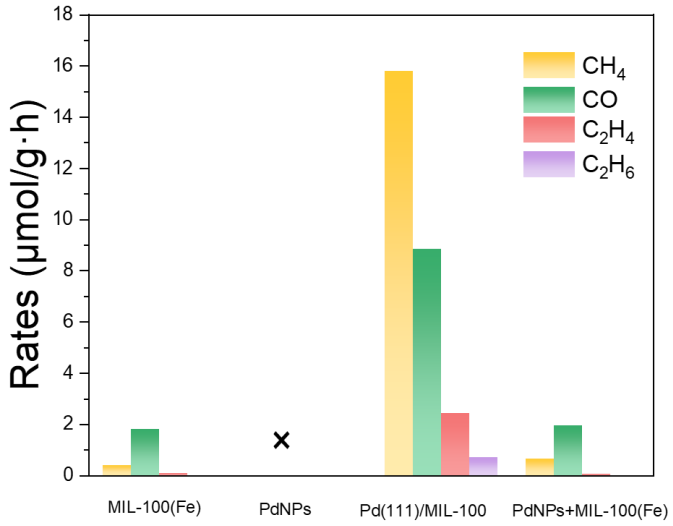

Fig. S19. Control experiments in several conditions for varied catalysts.

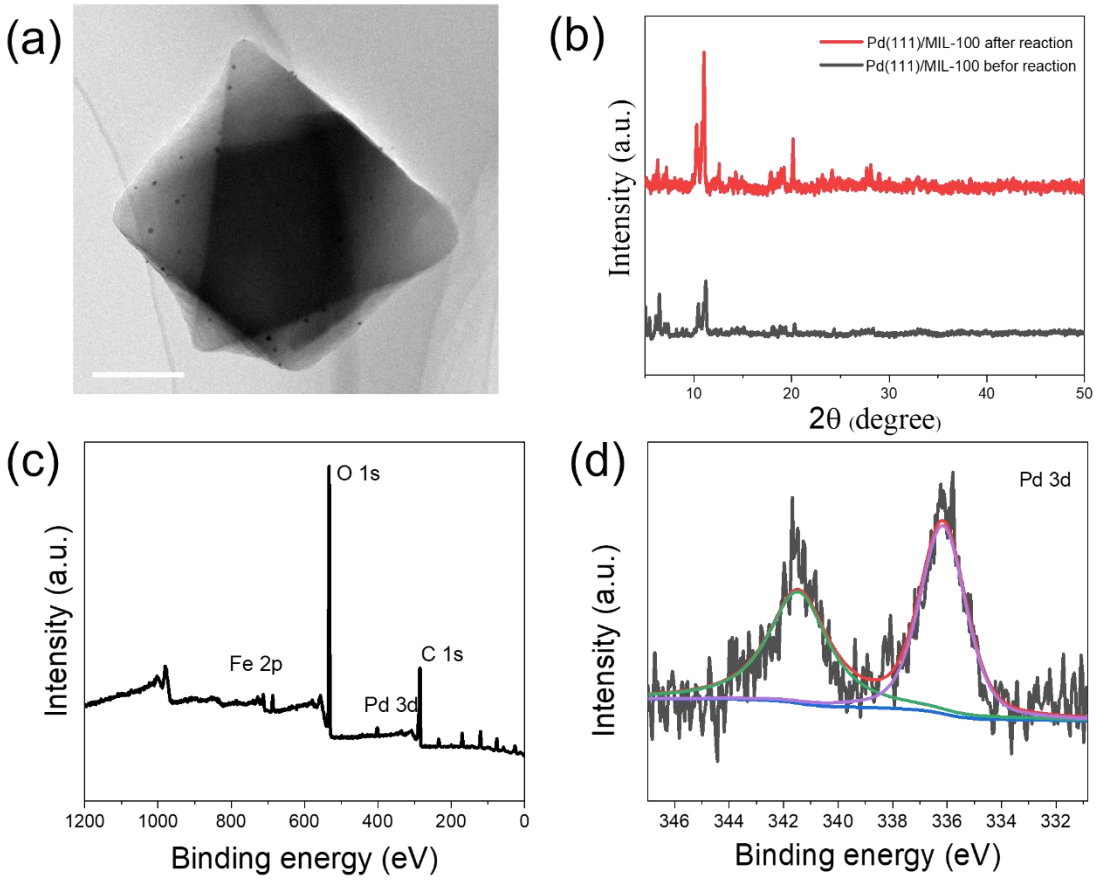

Fig. S20. (a) TEM image of Pd(111)/MIL-100 after cyclic test (scale bar: 500 nm). (b) PXRD pattern. (c) XPS survey spectra. (d) High-resolution Pd 3d XPS spectra.

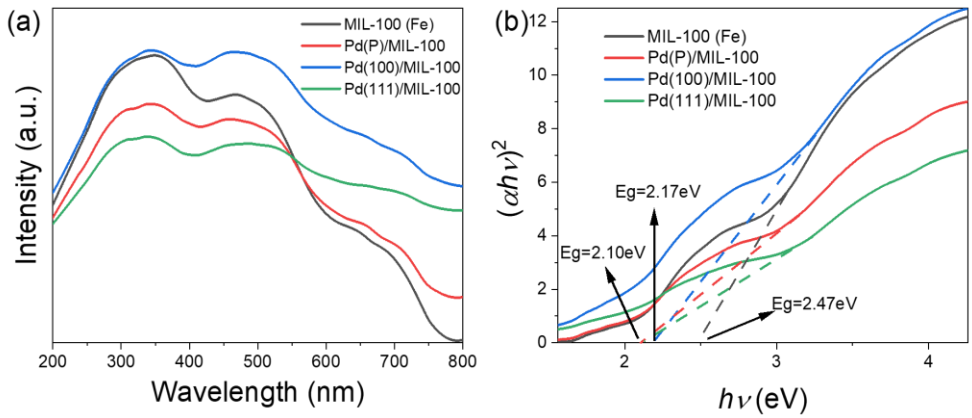

Fig. S21. (a) UV−vis diffuse reflectance spectra and (b) corresponding Tauc plots of the varied catalysts.

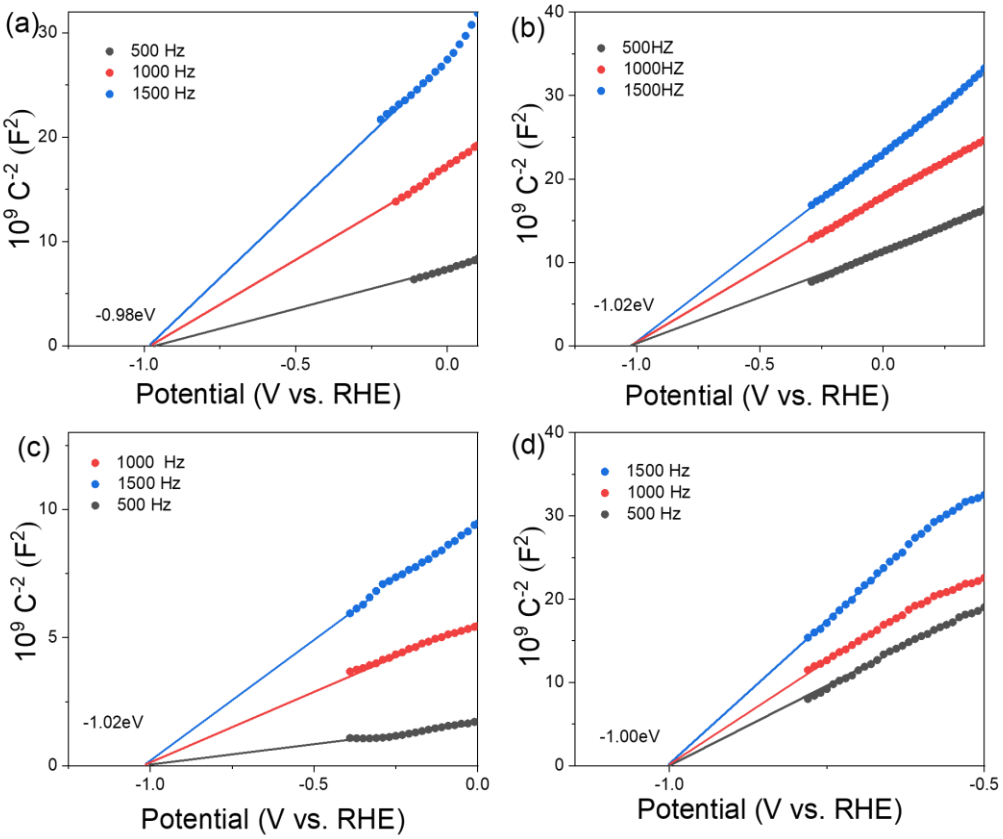

Fig. S22. Mott-Schottky plots of the varied catalysts. (a) MIL-100(Fe); (b) Pd(111)/MIL-100; (c) Pd(100)/MIL-100; (d) Pd(P)/MIL-100.

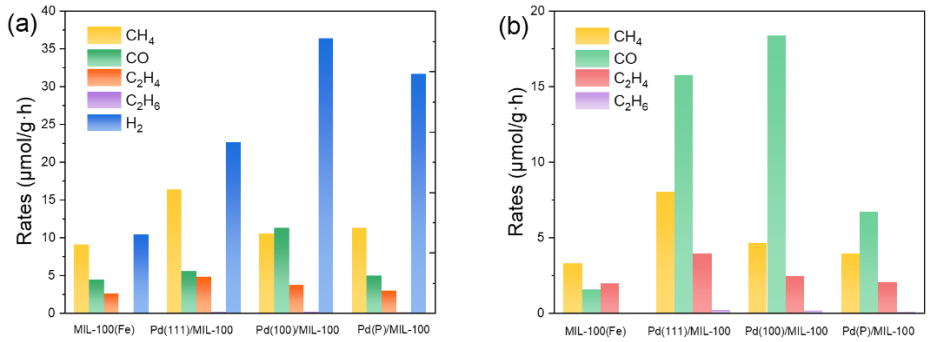

Fig. S23. Product formation rates for various catalysts in the photocatalytic CO_2 reduction using (a) TEA and (b) TEOA as sacrificial agents.

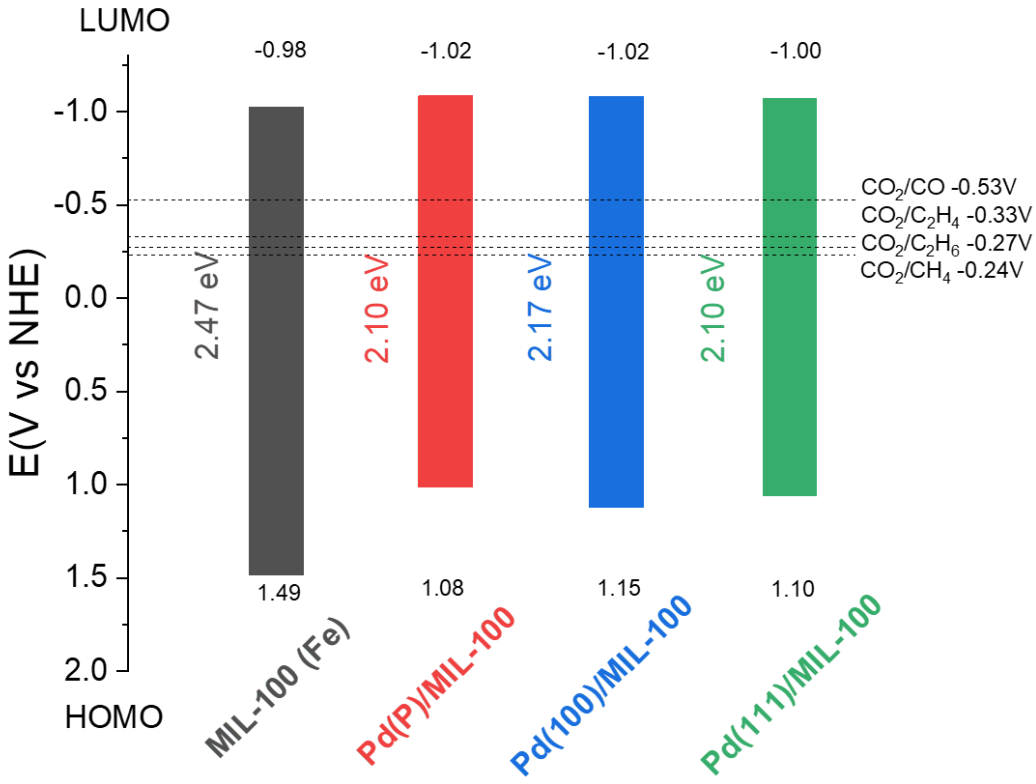

Fig. S24. HOMO−LUMO gap of the varied catalysts.

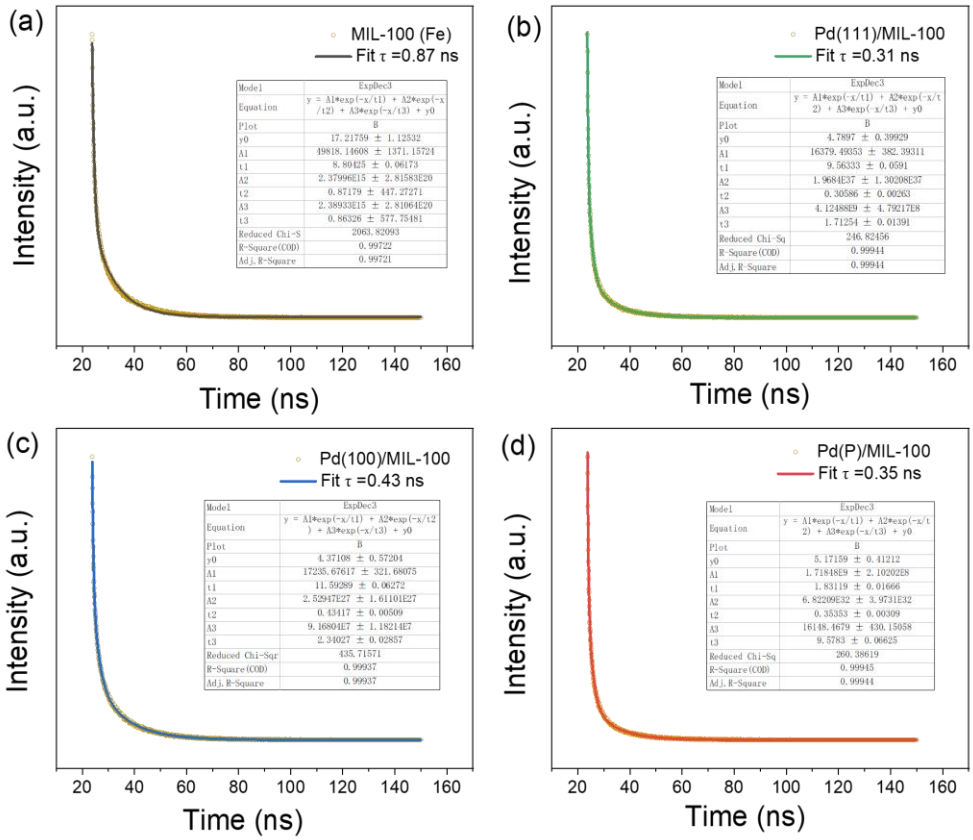

Fig. S25. Time-resolved fluorescence decay spectra of varied catalysts. (a) MIL-100(Fe); (b) Pd(111)/MIL-100; (c) Pd(100)/MIL-100; (d) Pd(P)/MIL-100.

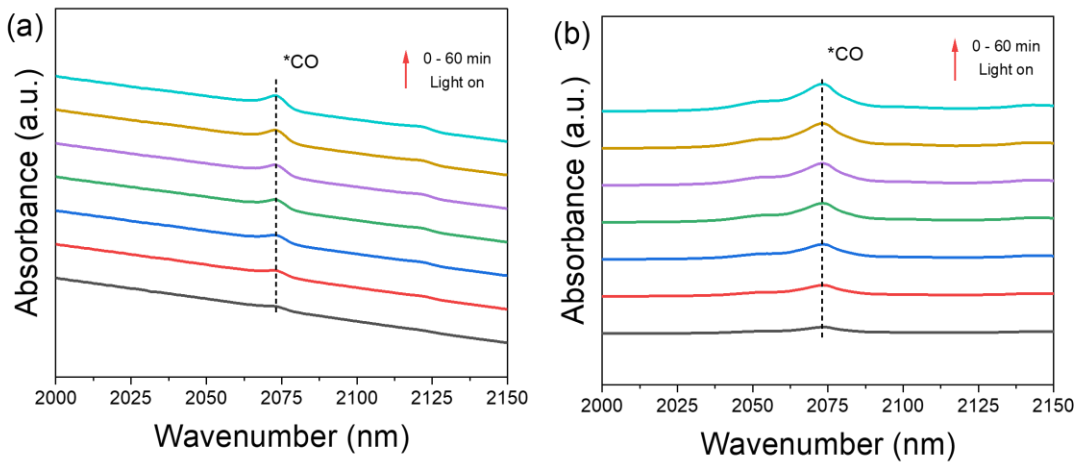

Fig. S26. Locally amplified *In situ* FT-IR spectra of CO_2 reduction under simulated light from 0 to 60 min for (a) Pd(100)/MIL-100 and (b) Pd(111)/MIL-100.

Table S1. Mass percentages of Pd elements in varied catalysts based on ICP-MS technology.

sample	Pd(111) mass loading (wt %)	Pd(100) mass loading (wt %)
0.3 wt % Pd/MIL-100	0.29	0.28
0.6 wt % Pd/MIL-100	0.61	0.59
0.9 wt % Pd/MIL-100	0.89	0.87
1.2 wt % Pd/MIL-100	1.19	1.20
1.9 wt % Pd/MIL-100	1.87	1.88

Table S2. Comparison of CO_2 reduction performance of the reported photocatalysts.

Photocatalyst	Light source	Wavelength (nm)	Sacrificial agent	Production rate (μmol/g•h)	Ref.
Pd(111)/MIL-100	300 W Xe lamp	AM 1.5	H_2O	CO 8.83, CH_4 15.79, **C_2H_4 2.4 C_2H_6 0.71**	**This work**
Pd(100)/MIL-100	300 W Xe lamp	AM 1.5	H_2O	CO 10.7, CH_4 1.39, **C_2H_4 0.28**	**This work**
Pd(P)/MIL-100	300 W Xe lamp	AM 1.5	H_2O	CO 2.21, CH_4 0.9, **C_2H_4 0.11**	**This work**
MIL-100(Fe)	300 W Xe lamp	AM 1.5	H_2O	CO 1.81, CH_4 0.4, **C_2H_4 0.08**	**This work**
CuO_X/p-ZnO	300 W Xe lamp	320−780	H_2O	CO 3.3, CH_4 2.2, **C_2H_4 2.7**	5
PD-Au_6Pd_1	300 W Xe lamp	---	H_2O	CO 10.9, CH_4 12.7, **C_2H_4 0.7**, **C_2H_6 0.8**	6
In-TiO_2/g-C_3N_4	UV	365	/	CO 2.32, CH_4 7.31, **C_2H_4 1.4**	7
Co/g-C_3N_4-0.2 SAC	300 W Xe lamp	---	H_2O	CO 2.9, CH_4 3.4, **C_2H_4 1.1**, C_3H_6 1.4, CH_3OCH_3 3.3	8
Carbon-Decorated Cu_2O Nanorods	350 W Xe lamp	>420 nm	---	CH_4 0.11, **C_2H_4 0.15**	9
Sv-CZ50	300 W Xe lamp	>420 nm	H_2O	CO 5.8, **C_2H_4 0.8**	10
Nb-BBN120	UV	365	H_2O	CO 2.3 **C_2H_4** 0.1	11
TTCOF-Zn	300 W Xe lamp	>420 nm	H_2O	CO 12.3	12
PtO/TiO_2	300 W Xe lamp	300−400 nm	H_2O	CO 4.6, H_2 1.6	13

References:

1. F. Gong, H. Li, Q. Zhou, M. Wang, W. Wang, Y. Lv, R. Xiao, D. V. Papavassiliou, *Nano Energy*, 2020, **74**, 104922.

2. F. Gong, Z. Ding, Y. Fang, C. J. Tong, D. Xia, Y. Lv, B. Wang, D. V. Papavassiliou, J. Liao, M. Wu, *ACS Appl. Mater. Interfaces*, 2018, **10**, 14614–14621.

3. Y. Li, F. Gong, Q. Zhou, X. Feng, J. Fan, Q. Xiang, *Appl. Catal. B: Environ.*, 2020, **268**, 118381.

4. Q. Zhou, F. Gong, Y. Xie, D. Xia, Z. Hu, S. Wang, L. Liu, R. Xiao, *Fuel*, 2022, **310**, 122442.

5. W. Wang, C. Deng, S. Xie, Y. Li, W. Zhang, H. Sheng, C. Chen, J. Zhao, *J. Am. Chem. Soc.*, 2021, **143**, 2984–2993.

6. Q. Chen, X. Chen, M. Fang, J. Chen, Y. Li, Z. Xie, Q. Kuang, L. Zheng, *J. Mater. Chem. A*, 2019, **7**, 1334–1340.

7. J. Park, H. Liu, G. Piao, U. Kang, H. W. Jeong, C. Janáky, H. Park, *Chem. Eng. J.*, 2022, **437**, 135388.

8. M. Ma, Z. Huang, D. E. Doronkin, W. Fa, Z. Rao, Y. Zou, R. Wang, Y. Zhong, Y. Cao, R. Zhang, Y. Zhou, *Appl. Catal. B: Environ.*, 2022, **300**, 120695.

9. L. Yu, G. Li, X. Zhang, X. Ba, G. Shi, Y. Li, P. K. Wong, J. C. Yu, Y. Yu, *ACS Catal.*, 2016, **6**, 6444–6454.

10. F. Tian, H. Zhang, S. Liu, T. Wu, J. Yu, D. Wang, X. Jin, C. Peng, *Appl. Catal. B: Environ.*, 2021, **285**, 119834.

11. J. A. Oliveira, J. A. Torres, R. V. Gonçalves, C. Ribeiro, F. G. E. Nogueira, L. A. M. Ruotolo, *Mater. Res. Bull.*, 2021, **133**, 111073.

12. M. Lu, J. Liu, Q. Li, M. Zhang, M. Liu, J. L. Wang, D. Q. Yuan, Y. Q. Lan, *Angew. Chem. Int. Ed.*, 2019, **58**, 12392–12397.

13. J. Wang, Y. Li, J. Zhao, Z. Xiong, J. Zhang, Y. Zhao, *PCCP.*, 2021, **23**, 9407–9417.